Received: 30 March 2020 | Revised: 15 June 2020 | Accepted: 16 June 2020

DOI: 10.1002/mrm.28415

FULL PAPER

Magnetic Resonance in Medicine

Ultra-high spatial resolution BOLD fMRI in humans using combined segmented-accelerated VFA-FLEET with a recursive RF pulse design

Avery J. L. Berman[1,2] | **William A. Grissom**[3,4] | **Thomas Witzel**[1,2] | **Shahin Nasr**[1,2] | **Daniel J. Park**[1] | **Kawin Setsompop**[1,2,5] | **Jonathan R. Polimeni**[1,2,5]

[1]Athinoula A. Martinos Center for Biomedical Imaging, Massachusetts General Hospital, Charlestown, Massachusetts, USA

[2]Department of Radiology, Harvard Medical School, Boston, Massachusetts, USA

[3]Vanderbilt University Institute of Imaging Science, Vanderbilt University, Nashville, Tennessee, USA

[4]Department of Biomedical Engineering, Vanderbilt University, Nashville, Tennessee, USA

[5]Harvard-MIT Division of Health Sciences and Technology, Massachusetts Institute of Technology, Cambridge, Massachusetts, USA

Correspondence
Avery J. L. Berman, Athinoula A. Martinos Center for Biomedical Imaging, Massachusetts General Hospital, 149 13th Street, Room 2301, Charlestown, MA 02129, USA.
Email: ajberman@mgh.harvard.edu

Funding information
Canadian Institutes of Health Research, Grant/Award Number: MFE-164755; National Institute of Biomedical Imaging and Bioengineering, Grant/Award Number: P41-EB015896, R01-EB016695, R01-EB019437 and U01-EB025162; National Center for Research Resources, Grant/Award Number: S10-RR019371 and S10-RR023043; National Institute of Mental Health, Grant/Award Number: R01-MH111419; National Eye Institute, Grant/Award Number: R01-EY026881

Purpose: To alleviate the spatial encoding limitations of single-shot echo-planar imaging (EPI) by developing multi-shot segmented EPI for ultra-high-resolution functional MRI (fMRI) with reduced ghosting artifacts from subject motion and respiration.

Theory and Methods: Segmented EPI can reduce readout duration and reduce acceleration factors, however, the time elapsed between segment acquisitions (on the order of seconds) can result in intermittent ghosting, limiting its use for fMRI. Here, "FLEET" segment ordering, where segments are looped over before slices, was combined with a variable flip angle progression (VFA-FLEET) to improve inter-segment fidelity and maximize signal for fMRI. Scaling a sinc pulse's flip angle for each segment (VFA-FLEET-Sinc) produced inconsistent slice profiles and ghosting, therefore, a recursive Shinnar-Le Roux (SLR) radiofrequency (RF) pulse design was developed (VFA-FLEET-SLR) to generate unique pulses for every segment that together produce consistent slice profiles and signals.

Results: The temporal stability of VFA-FLEET-SLR was compared against conventional-segmented EPI and VFA-FLEET-Sinc at 3T and 7T. VFA-FLEET-SLR showed reductions in both intermittent and stable ghosting compared to conventional-segmented and VFA-FLEET-Sinc, resulting in improved image quality with a minor trade-off in temporal SNR. Combining VFA-FLEET-SLR with acceleration, we achieved a 0.6-mm isotropic acquisition at 7T, without zoomed imaging or partial Fourier, demonstrating reliable detection of blood oxygenation level-dependent (BOLD) responses to a visual stimulus. To counteract the increased repetition time from segmentation, simultaneous multi-slice VFA-FLEET-SLR was demonstrated using RF-encoded controlled aliasing.

Conclusions: VFA-FLEET with a recursive RF pulse design supports acquisitions with low levels of artifact and spatial blur, enabling fMRI at previously inaccessible spatial resolutions with a "full-brain" field of view.

KEYWORDS

BOLD, FLEET, fMRI, high spatial resolution, multi-shot EPI, segmented EPI, SMS, variable flip angle

1 | INTRODUCTION

The pursuit of functional MRI (fMRI) acquisitions with high spatial resolution has been motivated by the need to better resolve functional activation across the fundamental processing units of the brain,[1,2] such as the layers[3,4] and columns[5,6] of the cerebral cortex, and subcortical and brainstem nuclei.[7] These structures are spatially organized at or below the millimeter scale,[8] necessitating submillimeter voxel sizes to properly resolve them. Moreover, there is mounting evidence that aspects of the hemodynamic response to neural activity are more finely regulated in space and time[9-11] than once believed,[12] suggesting that gains in fMRI spatial specificity can be made if images can be encoded with higher spatial resolution.

Higher spatial resolution in MRI is achieved by increased encoding in k-space. For two-dimensional (2D) multi-slice echo-planar imaging (EPI) and three-dimensional (3D) EPI, the most common fMRI readouts for high-resolution fMRI, this implies increases in the echo-train length, the total readout duration, and the minimum achievable echo time (TE), resulting in increased geometric distortion,[13] T_2^*-induced spatial blurring,[14,15] and often decreased blood oxygenation level-dependent (BOLD) sensitivity.[16] Accelerated parallel imaging techniques[17,18] can partially mitigate these effects, however achieving submillimeter resolution with 2D- or 3D-EPI readouts requires prohibitively high in-plane acceleration factors, even for modern RF coil arrays, resulting in unresolved aliasing artifacts and substantial reductions in the signal-to-noise ratio (SNR) through reduced signal averaging and g-factor noise amplification. This spatial encoding burden imposed by high-resolution imaging has become a major limitation for performing fMRI at submillimeter resolution with current gradient hardware performance, necessitating alternative imaging strategies.[19,20]

Two strategies for reducing the readout duration per excitation include zoomed imaging and multi-shot, in-plane segmented EPI. Zoomed imaging techniques, using either inner volume excitation[21,22] or outer volume suppression,[22-24] can overcome encoding limitations by restricting the phase-encode (PE) field of view (FOV), which reduces the number of required encoding steps along the PE direction. However, zoomed imaging has reduced SNR, increased specific absorption rate (SAR), and generally cannot detect simultaneous activation across distant brain regions due to the restricted FOV.[25] Multi-shot 2D-EPI acquires the data for each slice across multiple excitations, resulting in less encoding required per shot, reduced distortion and spatial blurring.[26] In contrast to zoomed imaging, multi-shot EPI allows an unrestricted, "full-brain" FOV that can cover the entire brain along the phase-encode dimension. For these reasons, prior to the widespread use of parallel imaging, multi-shot gradient-echo EPI was an attractive option for high-resolution fMRI.[27-32] Drawbacks of segmented 2D-EPI readouts include an increased volume repetition time (TR), which reduces statistical efficiency,[33] and shot-to-shot signal variations that result in intermittent ghosting artifacts that corrupt the fMRI time series. These coherent ghosting artifacts arise from the relatively long delay between the acquisition of segments for each slice (equal to the TR, which is on the order of seconds), making multi-shot 2D-EPI particularly vulnerable to motion and respiration-induced B_0 field changes that can occur between shots.[34]

FLEET (Fast Low-angle Excitation Echo-planar Technique) is a variation of segmented 2D-EPI with reduced vulnerability to inter-segment motion and field changes.[35] The time between segments is minimized by acquiring all segments of a given slice sequentially in time, without delay, before proceeding to the next slice. The method uses a constant low flip angle and several preparatory dummy pulses at the beginning of each slice's acquisition to achieve consistent signal levels between segments. This may be acceptable when high image SNR is not required, such as for GRAPPA auto-calibration data[36]; however, SNR should be maximized for the primary imaging data itself, and the time required for the dummy pulses every repetition is costly. To avoid these problems, a variable flip angle progression can be combined with the FLEET reordered readout, referred to here as *VFA-FLEET*, such that the imaging signal is maximized, and, ideally, a consistent signal level is achieved across all segments without dummy pulses.[37]

In practice, VFA-FLEET produces consistent magnetization at the center of each slice; however, the remainder of the slice profile systematically varies across shots.[38,39] This results in varying signal levels across segments that produce stable image artifacts, such as ghosting, that can be partly corrected during image reconstruction using one-dimensional navigators.[40,41] Strategies to prospectively mitigate the signal discrepancy across shots include empirically finding alternative flip angles that give stable signal levels[42] and varying the slice-select gradient amplitude to reduce the excitation bandwidth from shot-to-shot[43]; however, both strategies still result in varying slice profiles across shots that could produce inconsistent tissue contributions. Ideally, the slice profile should be matched across all shots.[38]

In this study, we implement combined segmented-accelerated 2D VFA-FLEET for ultra-high-resolution human fMRI with consistent slice profiles across segments. To achieve this, we have developed a recursive RF pulse design scheme using the Shinnar-Le Roux (SLR) algorithm.[44] We assess the temporal stability of the VFA-FLEET method with our SLR pulses and compare this to VFA-FLEET using the vendor's excitation RF pulse scaled to the desired variable flip angles and to conventional segmented EPI. We then demonstrate the ability to detect functional activation at 0.6-mm isotropic resolution using the proposed sequence without the use of partial Fourier undersampling or partial-FOV zoomed imaging. Finally, a simultaneous multi-slice (SMS) version of VFA-FLEET was implemented to counteract the reduced temporal sampling rate resulting from segmentation. A preliminary account of this study has been presented in abstract form.[45]

2 | THEORY

2.1 | Recursive RF pulse design

In VFA-FLEET, interleaved segments of EPI readouts are acquired consecutively, with no delay between them, as depicted in Figure 1. Because of the short recovery times between RF pulses in VFA-FLEET (~50–80 ms), there is negligible time for longitudinal relaxation and hence it is ignored, and the longitudinal magnetization available immediately before each RF excitation pulse is a function of both the previous excitation pulse's rotation parameters and the longitudinal magnetization available immediately before the previous excitation pulse. Thus, the longitudinal magnetization profile changes between excitations must be accounted for in the RF pulse design in order to maintain a consistent transverse magnetization (signal) profile across the imaged slice.

There are two boundary conditions for this problem, depicted in Figure 1D:

1. Because longitudinal magnetization (M_z) for a given slice is replenished during the long delay between the last segment of one acquisition and the first segment of the next, we assume $M_z = 1$ before the first excitation pulse (corresponding to the first segment).
2. The last excitation pulse (corresponding to the last segment) should have a 90° flip angle to maximize signal by depleting the remaining longitudinal magnetization.

We start by designing the first pulse. Designing this pulse requires knowledge of its nominal passband flip angle, which can be calculated recursively starting with the last flip angle as[37]:

$$\theta_{i-1} = \tan^{-1}\left(\sin\ \theta_i\right), \tag{1}$$

where i indexes segments. For a final flip angle of 90°, this gives, $\theta_i = 45°$ and 90° for a two-segment readout, and $\theta_i = 35.3°$, 45°, and 90° for a three-segment readout. Given the first pulse's flip angle, the conventional SLR algorithm can be used to calculate the first pulse. The SLR algorithm converts a target slice profile in M_{xy} and M_z into Cayley-Klein rotation parameters A and B.[44] A relates to the free precession due to the gradient field and B relates to the rotation around the RF field. A and B can be represented as polynomials whose coefficients give the desired RF pulse after application of the inverse SLR transform. The rotation parameters of the first pulse are denoted here by A^1 and B^1. We choose to absorb the phase of the A^1 polynomial into the B^1 polynomial to produce a flat phase slice profile. Given those parameters, if we ignore longitudinal relaxation between consecutive segments' excitations, the longitudinal magnetization before the second segment's pulse is:

$$M_z^{i+1} = M_z^i\left(1 - 2\left|B^i\right|^2\right). \tag{2}$$

To solve for the second segment's pulse, we need its complex-valued B profile. First, we solve for its magnitude, using the fact that the magnitude of the transverse magnetization (M_{xy}) it excites should be the same as the first pulse's magnitude, as:

$$\left|M_{xy}^1\right| = \left|M_{xy}^{i+1}\right| = \left|M_z^{i+1} 2\left(A^{i+1}\right)^* B^{i+1}\right| = \left|M_z^{i+1}\right| 2\sqrt{1 - \left|B^{i+1}\right|^2}\left|B^{i+1}\right|, \tag{3}$$

where the last equality results from the fact that $|A|^2 + |B|^2 = 1$. Squaring this equation, we get an equation that is quadratic in $\left|B^{i+1}\right|^2$, so the quadratic equation can be applied to solve for $\left|B^{i+1}\right|$. Then the complex-valued A^{i+1} can be solved by assuming a minimum-power pulse,[44] and the phase of B^{i+1} can be obtained from A^{i+1} and M_{xy}^1 as:

$$\angle B^{i+1} = \angle\left(\frac{M_{xy}^1}{M_z^{i+1} 2\left(A^{i+1}\right)^*}\right). \tag{4}$$

It is possible to take into account the effect of longitudinal relaxation between segments and/or between repetitions by modifying Equation (2), however, Bloch simulations, described below, showed minimal gain for the added complexity and, hence, relaxation effects are omitted in the design.

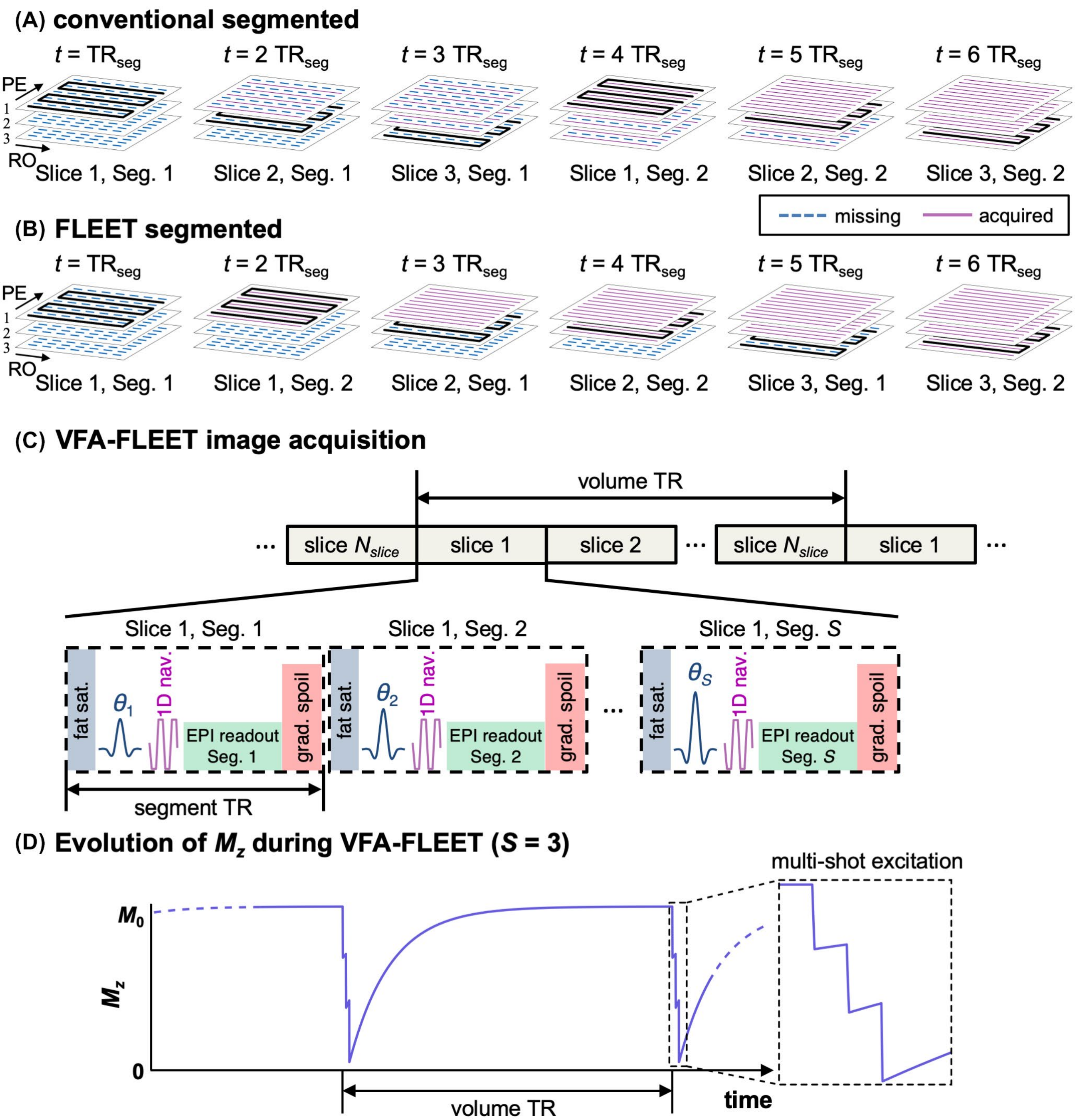

FIGURE 1 Comparison of segmentation orderings and depiction of the VFA-FLEET pulse sequence. A,B, Schematic of the acquisition of two segments across three slices, with time progressing from left to right, using conventional segmentation ordering where slices are acquired consecutively (A) or FLEET ordering where segments are acquired consecutively (B). Each plane represents a slice, dashed blue lines represent unacquired k-space lines, solid black lines represent the current acquired segment, and solid magenta lines represent previously acquired k-space lines. The labels above the slices denote the time elapsed at the end of each readout in units of segment TR (TR_{seg}). C, Schematic of the VFA-FLEET pulse sequence used for imaging. Each slice's S segments are acquired consecutively using flip angles from θ_1 to θ_S. D, Example evolution of M_z with T_1 relaxation for a single slice during VFA-FLEET with $S = 3$ ($\theta_i = 35.3°, 45°, 90°$). Dashed box shows a magnification of M_z around the multi-shot excitation period

This RF pulse design strategy is similar to one previously proposed by Kerr et al.[38,39] A difference between the two was that we cancelled the A polynomial phase, producing a more desirable slice profile. Moreover, ours is the first known experimental implementation of the design.

Since the first flip angle in VFA-FLEET dictates the image signal level, the image SNR is proportional to $\sin(\theta_1)$. Therefore, the SNR may be reduced relative to a single-shot or conventionally segmented sequence employing a larger flip angle, however, in the case of accelerated imaging, this loss in SNR may be offset by reducing the acceleration factor. The theoretical and experimental SNR of VFA-FLEET, including the impact of increased segmentation versus acceleration, is explored in detail in the Supporting Information, which is available online.

3 | METHODS

3.1 | Participants

Thirteen healthy adults volunteered to participate in the study (five females, ages 24–43). Prior to imaging, written informed consent was obtained from each participant in accordance with our institution's Human Research Committee. Four subjects participated in temporal stability measurements at 3T; five subjects participated in temporal stability measurements at 7T; one subject participated in a comparison of segmentation vs. acceleration (see Supporting Information) and the demonstration of SMS; and three subjects participated in an ultra-high-resolution task-based fMRI study.

3.2 | RF pulse implementation

The SLR RF pulse design was implemented in MATLAB R2017a (The MathWorks, Natick, MA) using the *rf_tools* library (http://rsl.stanford.edu/research/software.html). The first pulse was designed using the small-tip-angle approximation with $N = 1024$ points (polynomial order), time-bandwidth product (TBW) = 4, passband and stop-band ripples of 0.01% and 1%, respectively, and scaled to achieve the desired flip angle of the first pulse. As the longitudinal magnetization gets attenuated with each pulse, more high spatial frequency content is required in the subsequent pulses to achieve the target M_{xy} slice profile; therefore, the polynomial order of the subsequent pulses was scaled to 4× the initial pulse's order (ie, TBW increased to 4× the original). This was applied to the initial pulse by symmetrically zero-padding it to a length of 4096. Next, the algorithm outlined in the Theory section was implemented to calculate the subsequent RF pulses. However, to reduce the TBW to a more practical value, after each pulse was calculated, it was windowed using a Blackman filter outside the central 1.5× region, resulting in a final TBW = 6 for all pulses. After all pulses were computed, they were truncated to this central 1.5× region (1536 points). For slice thicknesses of 0.6 mm, 0.8 mm, and ≥1.0 mm, the implemented RF durations/bandwidths were 5.6/1.07, 4.2/1.43, and 4.0/1.5 ms/kHz, respectively. For reference, the duration and BW of the sinc pulse were 2.56 ms and 2.03 kHz (TBW = 5.2). MATLAB code that implements these designs is available at https://github.com/wgris som/vfa-fleet-RF.

To assess the performance of the proposed pulses, Bloch simulations of the slice profiles across shots were performed. The magnitude of the simulated slice profile integral $\left(\left|\int M_{xy}\right|\right)$ was computed for each shot as a metric for profile consistency. This slice profile integral reflects the total signal contribution per readout segment and is indicative of image artifacts, such as ghosting, that may arise due to shot-to-shot variations in slice profile. Additional simulations examining the impact of T_1 relaxation and non-ideal B_1^+ on the slice profiles and the impact of slice profile consistency on image temporal SNR (tSNR) are described in the Supporting Information.

3.3 | Acquisition

Experiments were conducted at 3T on a Siemens MAGNETOM TIMTrio using the vendor's body transmit coil and 32-channel receive head coil array (Siemens Healthcare, Erlangen, Germany) and at 7T on a Siemens MAGNETOM whole-body scanner equipped with SC72 gradients using an in-house built head-only birdcage volume transmit coil and 31-channel receive coil array. Segmented gradient-echo BOLD 2D-EPI time series were acquired with either a conventional segmented readout using the vendor's Hann-windowed sinc pulse, VFA-FLEET using the same sinc pulse scaled to the desired flip angles ("VFA-FLEET-Sinc"), or VFA-FLEET using the proposed SLR pulses ("VFA-FLEET-SLR"). Echo-time shifting was employed to reduce inter-segment discontinuities.[46] For each sequence, after each excitation, a three-line one-dimensional navigator was acquired for ghost corrections (see below). To suppress echo refocusing in VFA-FLEET, gradient spoiling was applied on the slice-select axis after each readout. For in-plane acceleration, FLEET-ACS data[36] with the maximum number of calibration lines (up to 128) were used for the auto-calibration scan with a constant 10° flip angle, $S \times R$ segments, five dummies per slice, minimum TE, and BW and echo-spacing matched to the imaging data.

B_1^+ spatial non-uniformity at 7T resulted in spatially varying ghost intensity levels in the VFA-FLEET images. This could be partly corrected during image reconstruction (see below), however, by a strategic choice of the reference transmit voltage, it was possible to reduce the overall ghost amplitude during acquisition (see Supporting Information Figures S4 and S5). Cerebrospinal fluid in the ventricles generally had the brightest signal and ghost intensity, and, therefore, was selected as the region of interest for the reference voltage. A B_1^+ map[47] was acquired for each subject and the reference voltage around the ventricles was determined online during the experimental session.

3.4 | Image reconstruction

All k-space data were reconstructed offline in MATLAB. Three ghost correction schemes were applied to the data: (i) *intra*-segment Nyquist ghost correction[48] was applied to each segment independently; (ii) *inter*-segment Nyquist ghost correction was applied to remove possible phase differences *across* segments and; (iii) *inter*-segment magnitude normalization was applied to account for possible shot-to-shot *intensity* differences. This latter correction used a scaling factor that minimized the sum-of-square residual between navigator magnitudes as

$$\underset{c_i}{\operatorname{argmin}} \left\| |I_{\mathrm{nav},1}| - c_i \, |I_{\mathrm{nav},i}| \right\|^2, \quad i = 2, \ldots, S, \tag{5}$$

where $I_{\mathrm{nav},i}$ represents the navigator intensity in position-space from the i-th shot. Following all ghost corrections, images from all channels were combined using root sum-of-squares. For accelerated acquisitions, data were reconstructed using GRAPPA[18] with a 3×4 kernel size, using the FLEET-ACS data with no regularization for kernel training, prior to coil combination. The corrections and reconstruction steps above were applied to VFA-FLEET-Sinc, VFA-FLEET-SLR, and conventional-segmented EPI.

3.5 | Assessing temporal stability

In this study, we categorize ghosting as either *stable* or *intermittent*, with the distinction being whether the ghost amplitude is constant across repetitions (stable) or not (intermittent). As temporal stability is paramount to the detection of neural activation with fMRI, it was chosen as the metric of interest for assessing the acquired data. This was done by acquiring 60 repetitions (plus dummies) of each sequence variant in subjects at rest then quantifying stability using tSNR, calculated voxel-wise as the mean signal intensity over time (μ) divided by the standard deviation over time (σ). However, tSNR alone did not reflect intermittent ghosting present in the segmented acquisitions and was biased by the underlying SNR, therefore, the temporal *skewness* was also calculated as

$$\text{skewness} = \frac{\left\langle (I(t) - \mu)^3 \right\rangle}{\sigma^3}, \tag{6}$$

where $I(t)$ is the signal intensity over time and $\langle\rangle$ denotes the temporal average. Skewness, which reflects the deviation of a voxel's intensity distribution from a symmetric distribution, is sensitive to spurious departures from the expected signal intensity, and, therefore, well-suited to quantify intermittent ghosting. Prior to calculating tSNR and skewness, the fMRI timeseries were motion corrected using AFNI *3dvolreg* v17.2.05[49] and had linear drift removed using FSL *fsl_glm* v5.0.7.[50]

Three different multi-shot sequences were compared (conventional-segmented, VFA-FLEET-Sinc, and VFA-FLEET-SLR) using two and three shots at both field strengths. The acquisition parameters are summarized in Table 1. At 7T, where B_0 inhomogeneity is more pronounced, the conventional-segmented acquisition used the minimum TR to reduce the likelihood of inter-segment phase errors, and the Ernst angle for $T_1 \approx 1500$ ms (intermediate T_1 of white matter and gray matter at 7T[51,52]). The TR varied between conventional-segmented and VFA-FLEET due to the need for gradient spoiling in VFA-FLEET.

Whole-brain tSNR and skewness were compared by co-registering the mean motion-corrected VFA-FLEET images to the mean motion-corrected conventional-segmented image using SPM12 *coreg*[53] and applying the corresponding transformations to the tSNR and skewness maps. Brain masks for each data set were then generated using FSL *BET*[54] and the intersection of the masks across acquisitions was used as the final brain mask.

3.6 | fMRI at ultra-high spatial resolution

To demonstrate that VFA-FLEET-SLR provides sufficient temporal stability to detect functional responses, and to showcase the capability of the combined segmented-accelerated acquisition to provide ultra-high spatial resolution with low distortion and blur, BOLD-weighted fMRI responses to a visual stimulus were measured in three subjects at 7T using a voxel size of 0.6 mm isotropic. The stimulus was a standard 8 Hz black-and-white flickering "dartboard" pattern presented for 4:30 min in 30 s on/off blocks with a neutral gray screen displayed during the off periods. The stimulus was projected on an in-bore screen and viewed by a mirror mounted inside the transmit coil. For this demonstration, 32 slices centered on the calcarine sulcus were acquired with a volume TR of 5.856 s, achieved with $S = 3$ and $R = 4$, therefore, 12-fold undersampling per segment. Acquisition details are given in Table 2. Three runs were collected for each subject.

Each run was motion-corrected as described above, then statistical activation maps were computed for each run independently with FSL *FEAT*.[55] No spatial smoothing nor pre-whitening were performed. The regressors consisted of the stimulus paradigm convolved with a gamma variate (3 s SD, 6 s mean lag) for the task regressor, as well as its temporal derivative and a linear drift as nuisance regressors. The mean motion-corrected images were co-registered to the middle run using FreeSurfer (v6.0.0) *mri_robust_register*,[56] the transformations were then applied to the statistical results, and a fixed-effects analysis was used to compute the net z-scores for each subject.

TABLE 1 Acquisition parameters for comparing the temporal stability of conventional-segmented and VFA-FLEET (sinc and SLR RF pulses) at 3T (top section) and 7T (bottom section)

	FOV (mm²)	Matrix	# slices	Flip angle(s) (degree)	TE (ms)	*R*	ACS lines	Segment TR (ms)	Volume TR (ms)	BW (Hz/pix)	Echo-spacing (ms)	Eff. echo-spacing (ms)	Gradient spoiling moment ($mT \cdot ms \cdot m^{-1}$)
3T 2.1-mm isotropic protocols													
2-shot													
Conventional-Segmented	200 × 200	96 × 96	30	90	30	1	*n/a*	2400	4800	2367	0.83	0.415	0
VFA-FLEET (sinc and SLR)	"	"	"	45, 90	"	"	"	80	4800	"	"	"	350
3-shot													
Conventional-Segmented	200 × 200	96 × 96	33	90	24	1	*n/a*	2380	7140	2367	0.75	0.25	0
VFA-FLEET (sinc and SLR)	"	"	"	35, 45, 90	"	"	“	72	7128	"	"	"	350
7T 1-mm isotropic protocols													
2-shot													
Conventional-Segmented	192 × 192	192 × 192	40	75	24	4	128	1940	3880	1240	1	0.125	0
VFA-FLEET (sinc and SLR)	"	"	"	45, 90	"	"	"	63	5040	"	"	"	500
3-shot													
Conventional-Segmented	192 × 192	192 × 192	40	75	24	4	128	1770	5310	1240	1	0.0833	0
VFA-FLEET (sinc and SLR)	"	"	"	35, 45, 90	"	"	"	59	7080	"	"	"	500

TABLE 2 VFA-FLEET-SLR acquisition parameters chosen for measuring BOLD fMRI responses to a visual stimulus at 0.6-mm isotropic (top section) and for testing the SMS acquisition and reconstruction at 0.8-mm isotropic resolution (bottom section)

# Segments	R	N_{MB}	FOV (mm^2)	Matrix	# Slices	Segment TR (ms)	Volume TR (ms)	Flip angles (degree)	TE (ms)	ACS lines	BW (Hz/pix)	Echo-spacing (ms)	Eff. echo-spacing (ms)	Gradient spoiling moment ($mT \cdot ms \cdot m^{-1}$)
0.6-mm isotropic fMRI protocol														
3	4	1	192 × 192	324 × 324	32	61	5856	35,45,90	27	128	965	1.27	0.106	0
0.8-mm isotropic SMS protocol														
2	3	2	192 × 192	240 × 240	78	74	5772	45,90	27	126	1157	1.01	0.168	500
2	3	2	"	"	42	"	3108	45,80	"	"	"	"	"	"
3	2	3	"	"	75	"	5550	35,45,90	"	"	"	"	"	"
3	2	3	"	"	39	"	2886	35,45,80	"	"	"	"	"	"
3	2	2	"	"	50	"	5550	35,45,90	"	"	"	"	"	"
3	2	2	"	"	30	"	3330	35,45,80	"	"	"	"	"	"

3.7 | Simultaneous multi-slice VFA-FLEET

In blipped controlled aliasing in parallel imaging (CAIPI),[57] which is commonly applied to improve the g-factor of *single-shot* EPI SMS acquisitions, gradient blips are applied on the slice axis during the readout to introduce an apparent FOV shift in the PE direction across slices. Here, by combining multi-band excitation with segmentation, it is possible to achieve the FOV shift by applying a slice-specific RF phase shift to each segment's excitation,[58] resulting in an apparent FOV/S shift between slices, and obviating the need for the gradient blips. The multi-band pulse for the n-th shot becomes

$$\mathrm{RF}_{\mathrm{MB},n}(t) = \mathrm{RF}_{\mathrm{SB},n}(t) \times \sum_{m=1}^{N_{\mathrm{MB}}} \exp\left\{-i\left(\Delta\omega_m t + \phi_m - \frac{(n-1)(m-1)2\pi}{S}\right)\right\}, \tag{7}$$

where $\mathrm{RF}_{\mathrm{SB},n}$ is the single-band RF pulse of the n-th shot, N_{MB} is the MB factor, $\Delta\omega_m$ is the centre frequency of the m-th slice, ϕ_m is a constant phase offset for each slice that reduces the peak power deposition,[59] and the final term in the exponential expresses the segment-wise FOV/S shift.

A flowchart of the slice-GRAPPA training/reconstruction pipeline is provided in Supporting Information Figure S7. To train the slice-GRAPPA kernels needed for SMS image reconstruction, single-band calibration data were acquired with no FOV shifts, but with otherwise identical scan parameters as the multi-band acquisition, that is, the calibration data were undersampled by R, as is standard, and VFA-FLEET was used for segmentation. Slice-GRAPPA training and image reconstruction followed a conventional single-shot SMS pipeline using one set of kernels per slice[57] with LeakBlock.[60] Further details on the slice-GRAPPA training and image reconstruction are provided in the Supporting Information. Because in-plane acceleration was also used, single-band FLEET-ACS data with $S \times R$ segments were acquired and used to train in-plane GRAPPA kernels, which were then applied after slice unaliasing and ghost corrections.

The SMS VFA-FLEET sequence and image reconstruction scheme was tested at a 0.8-mm isotropic resolution using three combinations of $S/R/N_{\mathrm{MB}}$ = 2/3/2, 3/2/3, 3/2/2, giving total accelerations of $R \times N_{\mathrm{MB}}$ = 6, 6, and 4, respectively. Two sets of multi-band acquisitions were performed: one where the number of acquired slices were set to achieve a volume TR of approximately 3 s, and another with increased slice coverage, giving a TR of ~5.7 s. Acquisition details are listed in Table 2.

4 | RESULTS

Figure 2 shows the simulated slice profiles for each shot of VFA-FLEET using scaled sinc pulses and the proposed

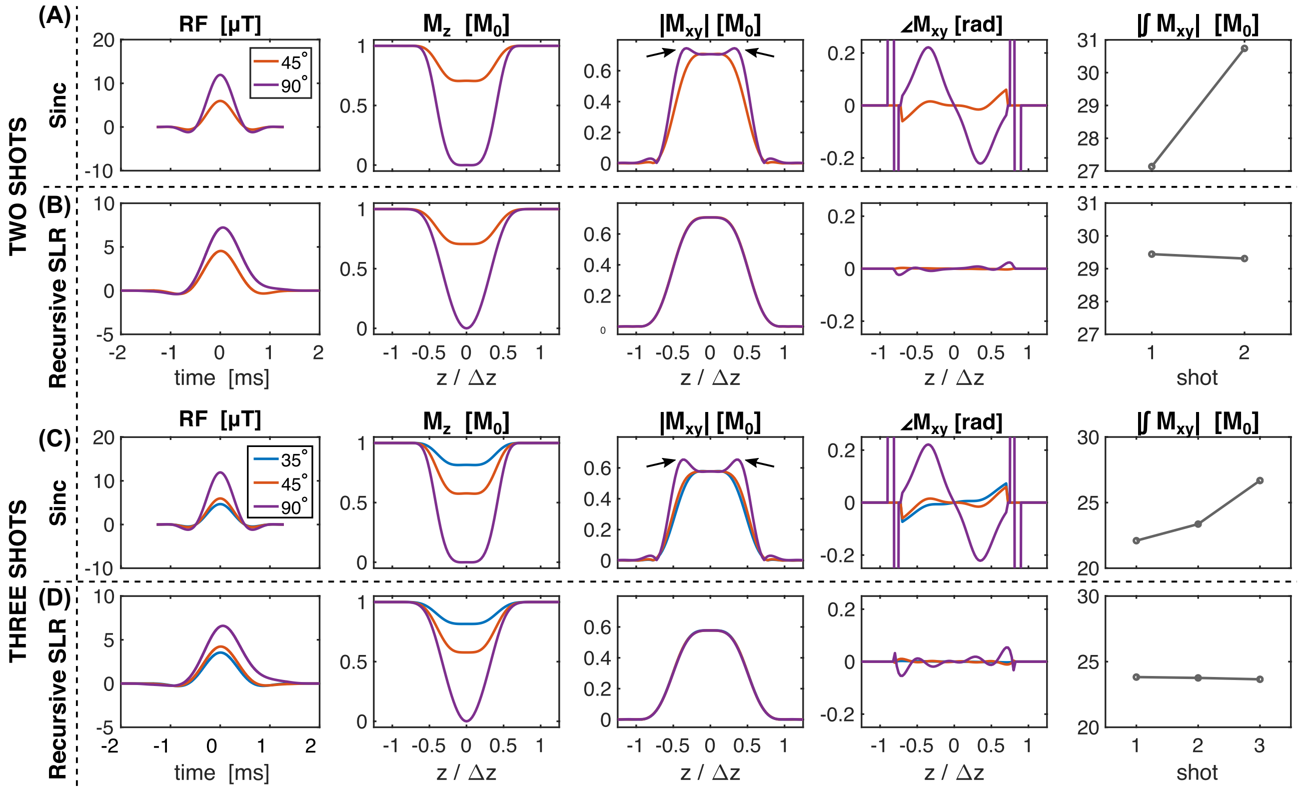

FIGURE 2 Simulated slice profiles across shots of VFA-FLEET using scaled sinc RF pulses (A,C) or the proposed recursive SLR pulses (B,D). Profiles were simulated for the two-shot case ($\theta_i = 45°, 90°$) (A,B) and the three-shot case ($\theta_i = 35°, 45°, 90°$) (C,D). Due to M_z being attenuated between shots (column 2), the sinc pulses generate non-uniform M_{xy} profiles in magnitude (column 3, A and C), phase (column 4, A and C), and integrated slice profile (column 5, A and C). Arrows in the $|M_{xy}|$ plots highlight this effect as it manifests as a horned profile. The SLR pulses properly account for this as evidenced by the consistent transverse slice profiles and integrals in (B) and (D). (For display purposes, the plotted phase is set to zero wherever $|M_{xy}| < 0.02$.)

recursively designed SLR pulses. For the scaled sinc pulses, the M_{xy} profiles become wider and have an increasing phase ramp with each shot, resulting in a horned slice profile for the 90° excitation as well as a 13% increase in the slice profile integral for two shots and a 21% increase after three shots. In contrast, for the SLR pulses, the M_{xy} profiles are nearly indistinguishable in magnitude and show minimal variation in phase, resulting in 0.5% and 0.7% decreases in slice profile integral for the two- and three-shot sequences, respectively. The recursive pulse design still produced consistent slice profiles when T_1 relaxation was incorporated into the Bloch simulations, despite ignoring relaxation in the pulse design (Supporting Information Figure S2); however, deviations from the nominal B_1^+ value had a large impact on the slice profile consistency (Supporting Information Figure S3), which impacts ghosting levels at ultra-high fields (Supporting Information Figures S4-S5). Based on simulations detailed in the Supporting Information, the slice profile broadening of VFA-FLEET-Sinc is expected to artifactually increase image tSNR by approximately 7% relative to VFA-FLEET-SLR for two shots and 13% for three shots (see Supporting Information Figure S6).

When examining the SLR waveforms in Figure 2, after the first shot, and in particular for the 90° excitation, the SLR pulses contain more RF energy near the end of the waveform, reflecting the fact that they must produce more high-frequency excitation to achieve the same out-of-slice to in-slice transitions as M_z is increasingly attenuated after each shot. As a consequence, the peak power and total energy of the SLR pulses are reduced relative to the scaled sinc pulses by 10% and 11% for two shots, respectively, and 25% and 16% for three shots after shortening the SLR pulse duration to 2.56 ms to match the duration of the sinc pulses (these differences are even more favorable for the VFA-FLEET-SLR pulses when calculated with the longer pulse durations actually implemented). Although the SAR limits were not reached in our experiments, this implies that the SAR of VFA-FLEET-SLR was less than for VFA-FLEET-Sinc, of relevance for the SMS implementation in particular.

Example reconstructions of a single image frame from data corresponding to the three segmentation variants at 3T are shown in Figure 3. These reconstructions demonstrate the reduction in stable ghosting in the VFA-FLEET acquisitions when replacing the scaled sinc pulses with the recursively designed SLR pulses. This artifact is further reduced

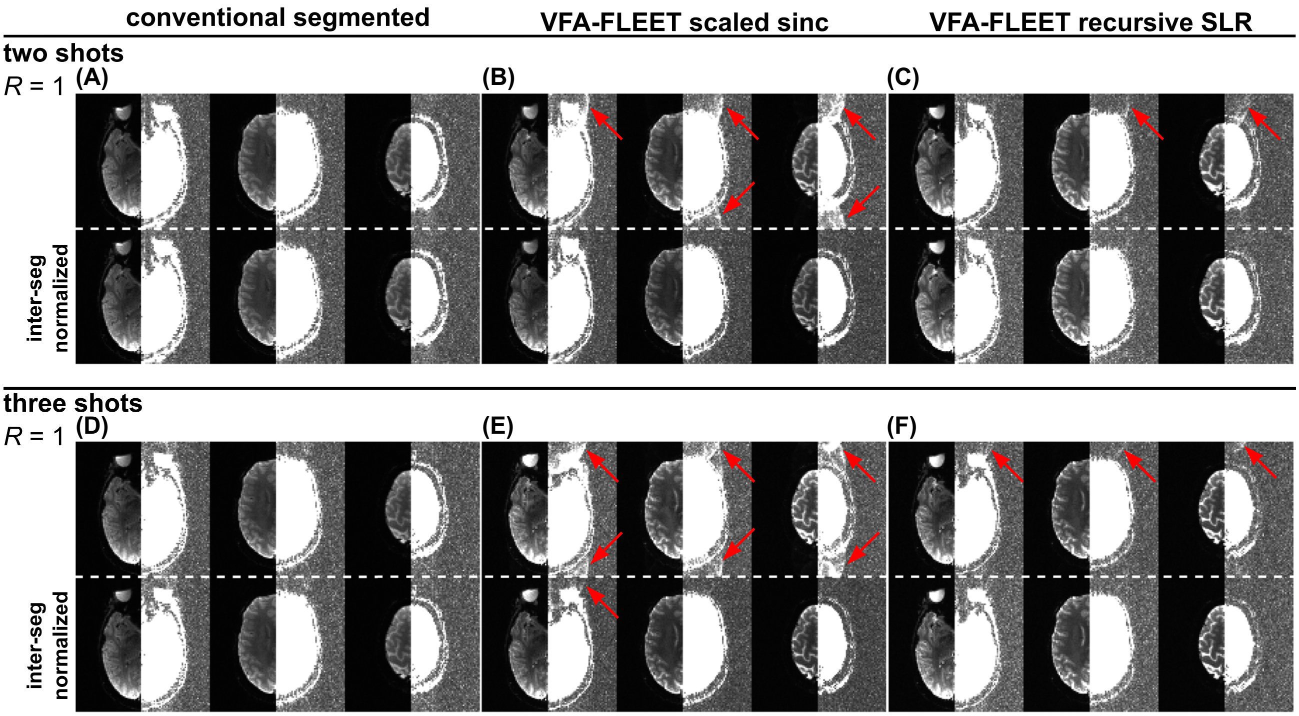

FIGURE 3 Examples of stable ghosting in reconstructions from a single subject scanned at 3T using conventional-segmented EPI (A,D), VFA-FLEET-Sinc (B,E), and VFA-FLEET-SLR (C,F) with either two shots (A–C) or three shots (D–F) and $R = 1$. All datasets were reconstructed with intra- and inter-segment phase correction, and the impact of adding inter-segment magnitude normalization is also displayed below the dashed lines. All images are individually windowed to have comparable contrast levels on the left halves and to highlight ghosts in the background on the right halves. Arrows highlight regions in the reconstructed images with notable stable ghosting artifacts resulting primarily from slice profile inconsistencies. There is no prominent ghost in the displayed conventional-segmented slices since, in general, conventional-segmented does not show stable ghosting, but rather intermittent ghosting

by the inter-segment magnitude normalization, particularly in the VFA-FLEET-Sinc images. There is no obvious ghost in the displayed conventional-segmented frame since, in general, conventional-segmented exhibits intermittent ghosting not stable ghosting, and at 3T, intermittent ghosting was most prominent in the case of subject head motion. See Supporting Information Videos S1-S4 for example time series in two subjects demonstrating varying degrees of stable and intermittent ghosting. One subject, shown in Supporting Information Videos S1 and S3, exhibited elevated levels of motion and was excluded from subsequent temporal stability analyses, despite the robustness to motion in the VFA-FLEET acquisitions.

Example reconstructions at 7T and the corresponding tSNR and skewness maps are shown in Figure 4, and additional example time series at 7T are provided in Supporting Information Videos S5-S8. When interpreting the skewness maps, note that regions with low SNR (eg, background and deep gray matter) have elevated skewness due to magnitude bias.[61] In the conventional-segmented image, there is intermittent ghosting visible across slices in the coronal and sagittal views, characterized by alternating light and dark slices in the reconstructed images (Figure 4A). This intermittent ghosting appears as sharp discontinuities and spatial nonuniformities in the tSNR and skewness maps and by overall elevated levels of skewness (positive and negative). Inter-segment magnitude normalization had no apparent impact in this case. For VFA-FLEET-Sinc, the reconstructed images show severe residual ghosting artifacts resulting from the intrinsic slice profile mismatch across shots. This artifact is substantially reduced by the inter-segment normalization, however not entirely, as evidenced by the slightly elevated skewness that remains after normalization. The recursive SLR pulses resulted in visibly improved image quality relative to the sinc pulses and inter-segment normalization further improved image quality, compensating for remaining slice-profile mismatches resulting from B_1^+ non-uniformity. Similarly, tSNR and skewness maps showed fewer sharp discontinuities, and the skewness magnitudes were reduced overall.

Group-average whole-brain tSNR and skewness from the three segmentation variants at 3T and 7T are plotted in Figure 5. At 3T, the group-averaged whole-brain tSNR was highest for the conventional-segmented acquisitions, due to their elevated flip angle, and comparable between the two VFA-FLEET variants. Nevertheless, the skewness was highest in conventional-segmented and substantially lower for the VFA-FLEET acquisitions, indicating improved temporal stability provided by VFA-FLEET. At 7T, conventional-segmented

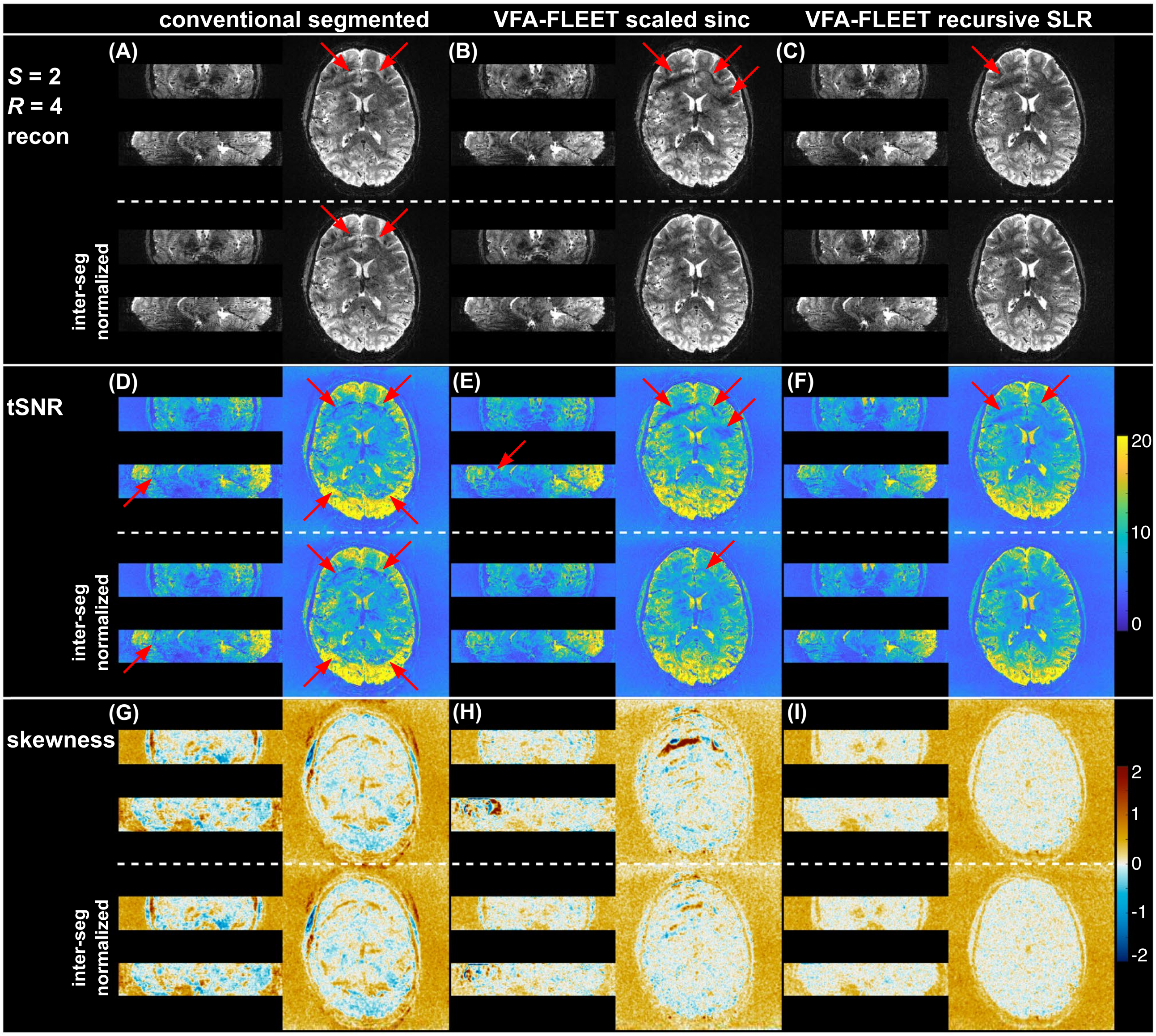

FIGURE 4 Example reconstructions from conventional-segmented EPI (A), VFA-FLEET-Sinc (B), and VFA-FLEET-SLR (C) acquired at 7T using two shots and $R = 4$ (ie, eightfold undersampling per shot). Maps of tSNR (D–F) and skewness (G–I) are also shown. All datasets were reconstructed with intra- and inter-segment phase correction, and the impact of adding inter-segment magnitude normalization is also displayed below the dashed lines. Arrows highlight regions in the reconstructed images and in the tSNR maps with notable ghosting artifacts and unresolved aliasing. In the skewness maps, the regions of notable ghosting are dark blue or dark orange if they are intermittent. Regions of low SNR (such as the background and deep gray matter) appear medium orange in skewness due to low-magnitude bias. The images in (A) through (C) are individually windowed to have comparable contrast levels. All tSNR maps share the colour bar on the far right and similarly for the skewness maps

and VFA-FLEET-Sinc had comparable tSNR and VFA-FLEET-SLR had the lowest tSNR. Some of this tSNR difference between the VFA-FLEET acquisitions can be explained by the undesired broadening of the slice profile that occurs with scaled sinc pulses (see Figure 2 and Supporting Information Figure S6). Skewness was greatest for conventional-segmented and comparable for the VFA-FLEET acquisitions. Across segmentation factors and field strengths, inter-segment normalization substantially reduced the skewness of VFA-FLEET-Sinc but at the expense of tSNR. Similar trends were observed for VFA-FLEET-SLR after inter-segment normalization but to a lesser extent, suggesting more consistent shot-to-shot magnitudes. All conventional-segmented scans were essentially unaffected by normalization, suggesting the instability was not adequately captured by the one-dimensional navigator-based phase and magnitude corrections.[62]

The results of the BOLD fMRI activation experiments imaged at 0.6-mm isotropic are shown in Figure 6. Average responses within the visual cortex across the three runs per participant are displayed overlaid on the mean VFA-FLEET-SLR image from a single run. Robust fMRI activation can

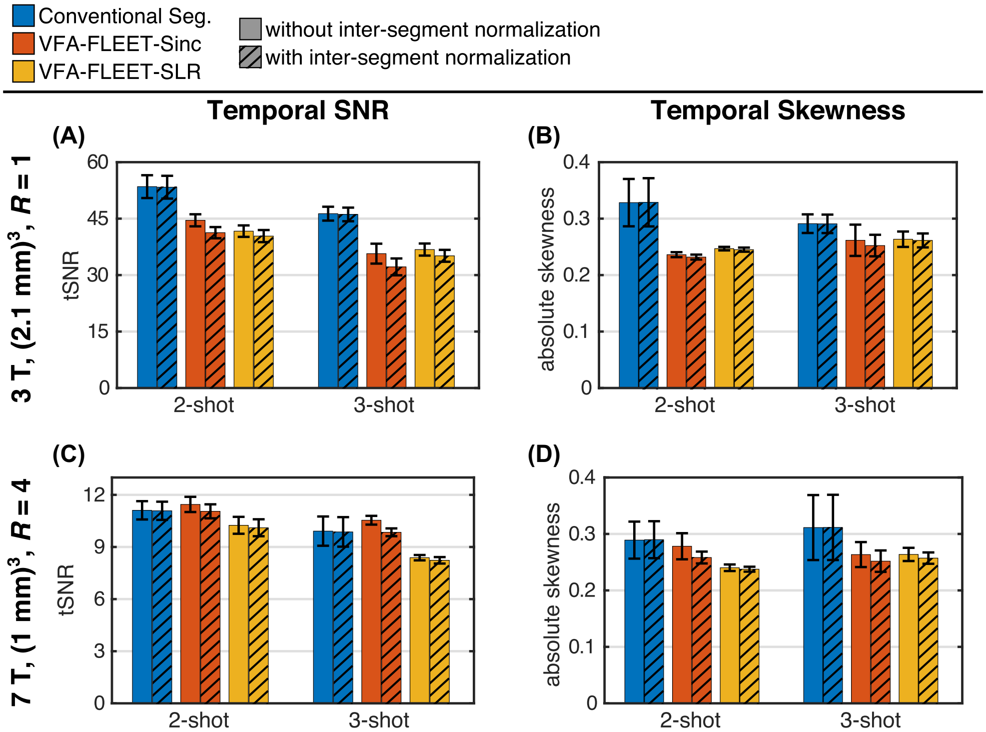

FIGURE 5 Mean whole-brain tSNR and absolute skewness across subjects at 3T (A,B) and 7T (C,D). (Note the different spatial resolutions and acceleration factors between 3T and 7T, labeled on the left.) Results from two- and three-shot conventional-segmented, VFA-FLEET-Sinc, and VFA-FLEET-SLR sequences are shown. All plots follow the legend at the top, where the hatchings distinguish the results from reconstructions performed with or without inter-segment magnitude normalization. Error bars show ± the standard error across subjects

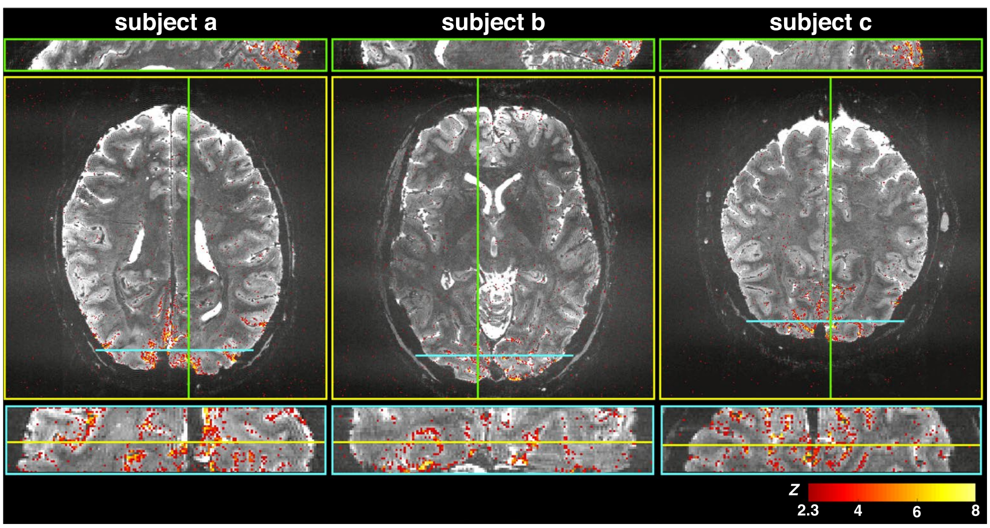

FIGURE 6 Activation maps demonstrating measured BOLD responses to visual stimulation from three subjects acquired at 0.6-mm isotropic resolution using VFA-FLEET-SLR with $S = 3$, $R = 4$ (ie, 12-fold undersampling per shot). For each subject, the mean Z-statistic maps across three runs (uncorrected) are displayed overlaid on the mean motion-corrected VFA-FLEET image from a single run. No spatial smoothing was applied. Varying degrees of slice obliquity were prescribed for each subject, as can be ascertained from the sagittal reformats in the top row. The coronal reformats in the bottom row are magnified 2× relative to the other views

be seen, demonstrating that there is sufficient temporal stability and detection sensitivity provided by this ultra-high-resolution fMRI acquisition.

Figure 7 shows the reconstruction from the 0.8-mm isotropic SMS acquisitions along with a single-band reference image. In the three $S/R/N_{MB}$ combinations, the TR ≈ 3 s

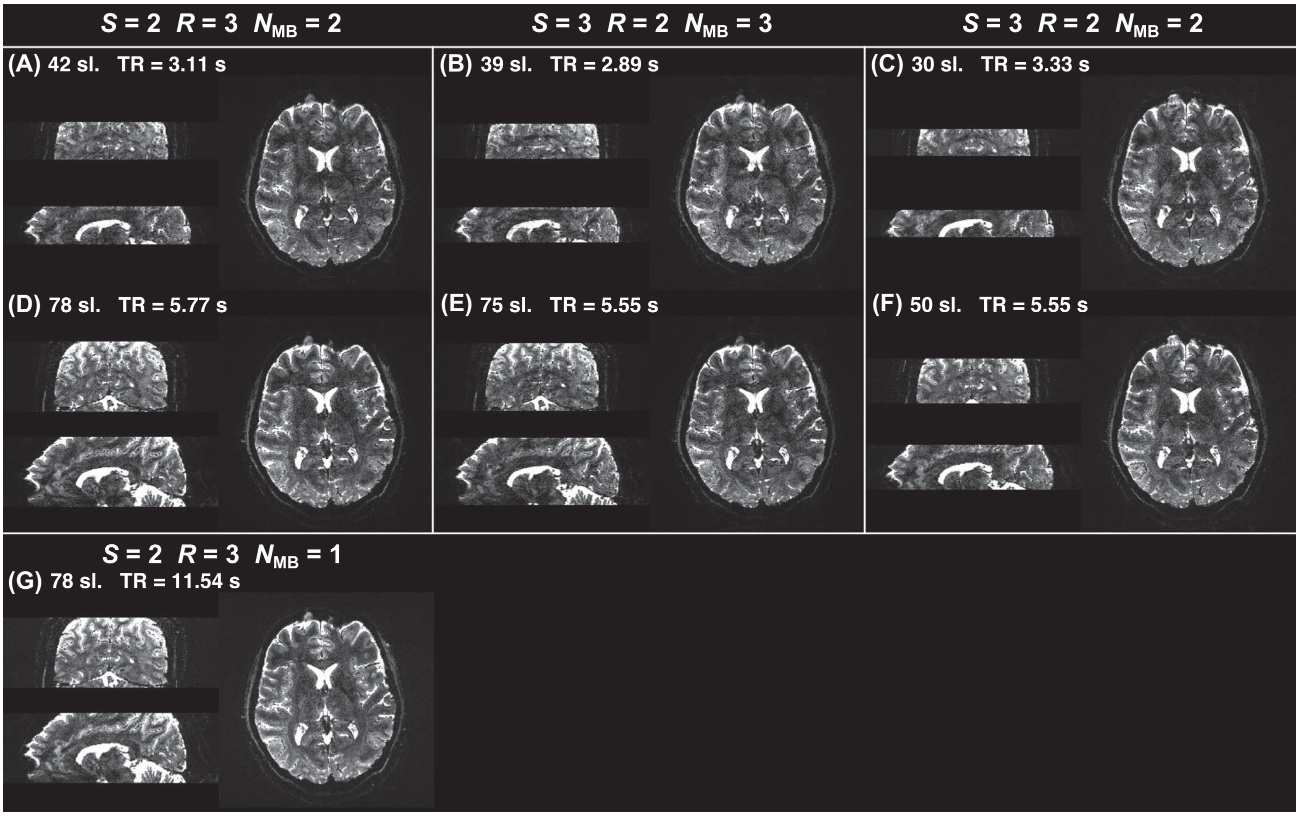

FIGURE 7 SMS reconstructions of single repetitions at 0.8-mm isotropic using VFA-FLEET-SLR. A–F, The top row shows the acquisitions with the slice number adjusted to achieve a TR ≈ 3 s and the bottom row shows the acquisitions with the expanded slice coverage to achieve a TR ≈ 5.7 s. The left column corresponds to $S/R/N_{MB}$ = 2/3/2, the middle column corresponds to 3/2/3, and the right column corresponds to 3/2/2. G, The single-band reference volume (after in-plane GRAPPA reconstruction) used for slice-GRAPPA kernel training of the acquisition in (D), shown for reference. Note, all acquisitions have matched in-plane undersampling per shot (ie, $S \times R = 6$)

acquisitions were all of relatively good quality given the high total acceleration and small slice separation between collapsed slices, with the least accelerated case of $S/R/N_{MB}$ = 3/2/2 (Figure 7C) showing the fewest artifacts. As expected, when the slice coverage was increased (Figure 7D-F), the image reconstructions were all improved and gave comparable quality to the single-band reference data.

To empirically test the impact of increased segmentation versus acceleration on image SNR, we reduced the acceleration factor and increased the segmentation factor (keeping the product $S \times R$ constant) while matching all other acquisition parameters. The results are summarized in the Supporting Information (and see Supporting Information Table S1 for acquisition details). By increasing the segmentation, the acceleration-related artifacts were significantly reduced, and image SNR was increased as predicted by Supporting Information Eq. [S3] due to the reduced g-factor noise, albeit at the cost of slice coverage (to achieve matched volume TR) (see Supporting Information Figure S1). Therefore, offsetting acceleration with segmentation can improve SNR, and the trade-off becomes one of temporal resolution/spatial coverage (related to S) vs. g-factor noise and unresolved aliasing (related to R).

5 | DISCUSSION

We have demonstrated a novel interleaved multi-shot EPI pulse sequence that combines FLEET segment ordering to reduce intermittent ghosting and a recursive RF pulse design to produce maximal signal while maintaining consistent signal intensity and slice profiles across shots.

5.1 | Temporal stability and ghosting comparisons

VFA-FLEET addresses the intermittent ghosting present in conventional-segmented EPI by acquiring segments in rapid succession. Ghosting in conventional-segmented arose when subjects moved or through respiration-induced field changes (particularly at 7T). Evidence of this ghosting is qualitatively evident in Figure 4 and the Supporting Information Videos. These artifacts were largely suppressed with VFA-FLEET. Despite the qualitative observations, the whole-brain average tSNR was typically greatest in the conventional-segmented acquisitions (Figure 5). This is because some regions are relatively unaffected by the ghosting and have high SNR due to the use of an elevated flip angle compared to VFA-FLEET, while other regions that overlap with the unstable ghosts have very low tSNR. However, because it is difficult to predict the exact anatomical locations where the ghosting will reduce the tSNR, many volumes in an fMRI time series would likely need to be "scrubbed," severely limiting the reliability of conventional-segmented sequences for use in fMRI, where spatially uniform or predictable sensitivity to brain activity is desired. VFA-FLEET can achieve a much more uniform sensitivity, albeit at the cost of global SNR due to its reduced flip angle.

In previous implementations of VFA-FLEET, a single RF waveform was scaled to achieve the desired flip angles, and it was known that the global signal intensity systematically varied across shots,[38,40,41,43,63-65] resulting in stable ghosting. Here, we have confirmed that inconsistency in slice profiles across shots was the main source of inter-segment signal variation. This was overcome by recursive RF pulse design using SLR theory (Figure 2), which improved image quality and skewness. However, VFA-FLEET-Sinc still had greater tSNR than VFA-FLEET-SLR. This was largely due to the slice profile broadening that occurs when scaling a single pulse (Figure 2). In our sequence implementation, the center line of k-space was acquired during the final excitation, which for VFA-FLEET-Sinc corresponds to the most broadened slice profile. Based on simulations (Supporting Information Figure S6), we estimate the broadening accounts for approximately 100%/116% of the difference in group-averaged tSNR for two/three shots at 3T and 96%/90% at 7T, with deviations of these values from 100% attributed to inter-run and inter-subject variability and B_0 and B_1^+ inhomogeneity. This will result in partial volume effects with neighboring slices and can be interpreted as a loss of spatial resolution in the slice direction.[43]

5.2 | FMRI at ultra-high spatial resolution

Using VFA-FLEET-SLR, we demonstrated BOLD activation to a visual stimulus at a nominal isotropic voxel size of 0.6 mm (Figure 6). Fracasso et al,[66] achieved a smaller voxel size of 0.55 mm isotropic using 3D-EPI for BOLD fMRI with the use of high-density surface coils, permitting the use of a restricted FOV. To the best of our knowledge, our study accomplished the highest spatial resolution for human fMRI using a whole-brain receive coil array, a full-brain field-of-view, no partial Fourier, and a body gradient coil, that is, the conditions for a typical ultra-high field fMRI study. This was enabled by 12-fold undersampling per shot ($S = 3$ and $R = 4$) but still required a relatively long readout per segment (34 ms) for the 192-mm FOV. Due to T_2^* decay during the acquisition, the in-plane spatial blurring was $\approx 0.01\% \times 7.7\%$ (readout × phase-encode) resulting in an effective voxel size of 0.60×0.65 mm^2,[15] assuming a tissue T_2^* of 25 ms.[29] Due to the reduced SNR at such high spatial resolution, the activation patterns were primarily localized to tissue surrounding large vessels near the pial surface, as expected.[67] Detection sensitivity could be improved by increasing the SNR during acquisition using a more spatially homogeneous B_1^+ excitation and increased transmit voltage (see below) or through data analysis strategies. It is common practice in laminar fMRI data analysis to spatially pool or smooth all voxels within a cortical depth range and region-of-interest to generate a laminar profile, which can boost the contrast-to-noise ratio.[68] Using smaller voxels reduces partial volume effects from cerebrospinal fluid and white matter that, when combined with anatomically informed smoothing, can lead to an increased contrast-to-noise ratio compared to data acquired at lower resolution.[69]

5.3 | Limitations and future work

VFA-FLEET relies on a precise schedule of excitation flip angles being delivered, such that B_1^+ non-uniformity results in regionally varying stable ghosting (Supporting Information Figures S4-S5). Despite the lack of uniformity at ultra-high field, in practice, the image quality of VFA-FLEET-SLR across the brain was perhaps higher than expected in the wide range of protocols tested at 7T. We aimed to mitigate B_1^+-related artifacts prospectively during acquisition by judicious choice of the transmit voltage and retrospectively during image reconstruction via inter-segment signal normalization. The transmit voltage selected was typically lower than what would produce the optimal SNR in cortex, therefore, this currently limits the sensitivity of VFA-FLEET at ultra-high field. This could be resolved using parallel RF transmission,[70] albeit at the expense of a more complicated workflow, potentially simplified through universal parallel-transmit pulses.[71]

We used inter-segment normalization to counteract the effects of B_1^+ non-uniformity. A scalar correction factor was applied to each segment, which reduced the overall ghost intensity, however, since B_1^+ varies in two-dimensions, this also led to increased ghosting in other areas, as seen in Supporting Information Figures S4-S5. A 2D intensity correction factor per shot could be estimated by acquiring an additional set of calibration scans to reconstruct an image for each shot and taking their ratios, or by measuring a B_1^+ map to estimate a signal intensity variation map per shot. These maps could further be incorporated into a forward-model reconstruction in a low-rank constrained reconstruction.[72,73]

FMRI at high spatial resolution incurs trade-offs in the temporal resolution and spatial coverage. Studies using block-design experimental paradigms with long stimulus presentations (eg, Refs. [4-6,74,75]) and jittered inter-stimulus intervals can cope with longer TRs, and conventional resting-state fMRI analyses only require a TR of 5 s to Nyquist-sample an upper frequency of 0.1 Hz. However, higher sampling rates can improve statistical power[76] and provide more flexibility in experimental design and resting-state analyses.[77] Robust BOLD responses to brief or rapidly oscillating stimuli can be detected when using so-called "fast" fMRI. Due to locally varying temporal lags in the BOLD response, the detection sensitivity of fast fMRI can be improved if partial volume averaging and excessive spatial smoothing are avoided.[11,78] The high spatial resolution VFA-FLEET protocols presented here could be adapted to achieve sufficient temporal resolution for fast fMRI while helping to reduce partial volume effects. The TR can be arbitrarily reduced by decreasing the number of slices acquired or by reducing the matrix size and using a smaller PE FOV. For example, the TR of the 0.6-mm protocol can be reduced from 5.856 s to 5 s by reducing the FOV from 192 mm to 154 mm. Additionally, considerable gradient spoiling was employed across all shots so as to maximize tSNR. Significant time savings and more effective spoiling could be achieved through further optimization of the spoiling, including removing the spoiler on the final shot.

Using SMS can help address both temporal resolution and spatial coverage limitations. We incorporated SMS with VFA-FLEET-SLR and showed preliminary data demonstrating its feasibility. Incorporating the CAIPI shift in the RF pulses themselves as in the original CAIPIRINHA method[79] can be advantageous for some protocols as it obviates the gradient blips required for single-shot blipped CAIPI,[58] which can limit the minimum achievable echo-spacing, especially for closely spaced slices, and, therefore, extend the readout duration. Moving to higher spatial resolution with increasing in-plane acceleration and thinner slices, the burden of decomposing the collapsed slices is placed more on the in-plane array elements, resulting in an ~$R \times N_{\mathrm{MB}}$ in-plane acceleration problem. With the reduced slice-FOV tested here (Figure 7A-C), the $R \times N_{\mathrm{MB}} = 6$ acquisitions produced reasonable looking acquisitions, although they likely pushed the limit of usability without employing a denser coil array.[80,81] Increasing the spatial separation between collapsed slices improved the reconstruction image quality (Figure 7D-F), as expected.[79] We are currently investigating improvements to the SMS acquisition and reconstruction, including adding gradient blips to enable arbitrary FOV shifts[82] and adapting the single slice-GRAPPA kernel used here to a multi-kernel approach that accounts for phase imperfections in odd/even k-space lines[83] and intensity differences across segments.

Finally, the proposed techniques are generalizable to contrasts and readouts beyond 2D gradient-echo BOLD EPI. VFA-FLEET has previously been combined with a short-TE centre-out 2D-EPI readout for T_1-weighted structural imaging[40] and arterial spin labeling (ASL) with reduced BOLD contamination.[65] These applications would benefit from the proposed recursive pulse design to improve the slice profile consistency. Currently, we are extending our methods to VFA-FLEET spin-echo imaging for T_2-weighted BOLD fMRI with reduced R_2' contamination[84] or motion-robust high-resolution diffusion MRI. 3D-EPI is another form of multi-shot EPI, with segmentation conventionally applied only along the partition-encoding dimension.[85] It too is commonly used for high-resolution fMRI as it tends to have elevated tSNR relative to 2D-EPI when thermal noise dominated.[85-89] For fMRI sequences that are not in a steady-state due to a contrast preparation, like VAscular Space Occupancy[88] or ASL,[90] the recursive pulse design could improve the slab profile consistency when using 3D-EPI readouts. Note, since 3D-EPI uses the same readout trajectory per partition as 2D-EPI, it is subject to the same *in-plane* spatial encoding limitations discussed throughout. Therefore, in-plane segmentation, in addition to partition segmentation, could be used to achieve ultra-high spatial resolution, although at the potential cost of increased vulnerability to motion and physiological noise contamination due to an increased volume-encoding time.[91]

6 | CONCLUSIONS

The aim of this study was to develop a pulse sequence for high-resolution fMRI that can overcome the current spatial encoding limitations of single-shot EPI. We developed a segmented EPI pulse sequence, VFA-FLEET, using recursively designed SLR RF pulses. FLEET segment ordering reduced the intermittent ghosting present in conventional-segmented EPI, and the recursive pulse design reduced the stable ghosting compared to VFA-FLEET using scaled sinc pulses, resulting in improved image quality. Combined, this enabled ultra-high spatial-resolution fMRI studies, without the use of partial Fourier or zoomed imaging, tested down to a voxel size of 0.6 mm isotropic achieved with three shots and 12-fold undersampling per shot, with low spatial blur and low levels of artifacts. To combat the increased volume TR, the VFA-FLEET acquisition was shown to be compatible with SMS where the CAIPI phase shifts were incorporated into the RF pulses, obviating the need for CAIPI gradient blips. In future work, we aim to improve the sequence's B_1^+ robustness and to explore additional image contrasts beyond gradient-echo BOLD.

ACKNOWLEDGMENTS

We thank Mr. Kyle Droppa and Ms. Nina Fultz for help with volunteer recruiting and MRI scanning, and Dr. Berkin Bilgic, Dr. Congyu Liao, and Dr. Mary-Kate Manhard for helpful discussions on SMS image acquisition and reconstruction. This work was supported in part by the CIHR (MFE-164755), the NIH NIBIB (grants P41-EB015896, R01-EB019437, and R01-EB016695), the NEI (grant

R01-EY026881) by the *BRAIN Initiative* (NIH NIMH grant R01-MH111419 and NIBIB grant U01-EB025162), and by the MGH/HST Athinoula A. Martinos Center for Biomedical Imaging; and was made possible by the resources provided by NIH Shared Instrumentation Grants S10-RR023043 and S10-RR019371.

DATA AVAILABILITY STATEMENT

MATLAB code that implements the recursive RF pulse design is available at https://github.com/wgrissom/vfa-fleet-RF.

ORCID

Avery J. L. Berman https://orcid.org/0000-0001-7631-1049
William A. Grissom https://orcid.org/0000-0002-3289-1827

REFERENCES

1. Rockland KS, Pandya DN. Laminar origins and terminations of cortical connections of the occipital lobe in the rhesus monkey. *Brain Res*. 1979;179:3-20.
2. Mountcastle VB. The columnar organization of the neocortex. *Brain*. 1997;120:701-722.
3. Polimeni JR, Fischl B, Greve DN, Wald LL. Laminar analysis of 7T BOLD using an imposed spatial activation pattern in human V1. *NeuroImage*. 2010;52:1334-1346.
4. Koopmans PJ, Barth M, Norris DG. Layer-specific BOLD activation in human V1. *Hum Brain Mapp*. 2010;31:1297-1304.
5. Yacoub E, Shmuel A, Logothetis N, Ugurbil K. Robust detection of ocular dominance columns in humans using Hahn Spin Echo BOLD functional MRI at 7 Tesla. *NeuroImage*. 2007;37:1161-1177.
6. Nasr S, Polimeni JR, Tootell RB. Interdigitated color- and disparity-selective columns within human visual cortical areas V2 and V3. *J Neurosci*. 2016;36:1841-1857.
7. Sclocco R, Beissner F, Bianciardi M, Polimeni JR, Napadow V. Challenges and opportunities for brainstem neuroimaging with ultrahigh field MRI. *NeuroImage*. 2018;168:412-426.
8. Dumoulin SO, Fracasso A, van der Zwaag W, Siero JCW, Petridou N. Ultra-high field MRI: Advancing systems neuroscience towards mesoscopic human brain function. *NeuroImage*. 2018;168:345-357.
9. Rungta RL, Chaigneau E, Osmanski BF, Charpak S. Vascular compartmentalization of functional hyperemia from the synapse to the Pia. *Neuron*. 2018;99:362-375.e4.
10. Longden TA, Dabertrand F, Koide M, et al. Capillary K(+)-sensing initiates retrograde hyperpolarization to increase local cerebral blood flow. *Nat Neurosci*. 2017;20:717-726.
11. Lewis LD, Setsompop K, Rosen BR, Polimeni JR. Fast fMRI can detect oscillatory neural activity in humans. *Proc Natl Acad Sci USA*. 2016;113:E6679-E6685.
12. Logothetis NK, Wandell BA. Interpreting the BOLD signal. *Annu Rev Physiol*. 2004;66:735-769.
13. Jezzard P, Balaban RS. Correction for geometric distortion in echo planar images from B0 field variations. *Magn Reson Med*. 1995;34:65-73.
14. Farzaneh F, Riederer SJ, Pelc NJ. Analysis of T2 limitations and off-resonance effects on spatial resolution and artifacts in echo-planar imaging. *Magn Reson Med*. 1990;14:123-139.
15. Haacke EM, Brown RW, Thompson MR, Venkatesan R. *Magnetic Resonance Imaging: Physical Principles and Sequence Design*, 1st edn. New York: John Wiley & Sons; 1999.
16. Buxton RB. *Introduction to Functional Magnetic Resonance Imaging: Principles and Techniques*, 2nd edn. Cambridge; New York: Cambridge University Press; 2009.
17. Pruessmann KP, Weiger M, Scheidegger MB, Boesiger P. SENSE: Sensitivity encoding for fast MRI. *Magn Reson Med*. 1999;42:952-962.
18. Griswold MA, Jakob PM, Heidemann RM, et al. Generalized autocalibrating partially parallel acquisitions (GRAPPA). *Magn Reson Med*. 2002;47:1202-1210.
19. Olman CA, Yacoub E. High-field FMRI for human applications: An overview of spatial resolution and signal specificity. *Open Neuroimag J*. 2011;5:74-89.
20. Polimeni JR, Wald LL. Magnetic resonance imaging technology-bridging the gap between noninvasive human imaging and optical microscopy. *Curr Opin Neurobiol*. 2018;50:250-260.
21. Feinberg DA, Hoenninger JC, Crooks LE, Kaufman L, Watts JC, Arakawa M. Inner volume MR imaging: Technical concepts and their application. *Radiology*. 1985;156:743-747.
22. Heidemann RM, Ivanov D, Trampel R, et al. Isotropic submillimeter fMRI in the human brain at 7 T: Combining reduced field-of-view imaging and partially parallel acquisitions. *Magn Reson Med*. 2012;68:1506-1516.
23. Pfeuffer J, van de Moortele P-F, Yacoub E, et al. Zoomed functional imaging in the human brain at 7 Tesla with simultaneous high spatial and high temporal resolution. *NeuroImage*. 2002;17:272-286.
24. Feinberg D, Chen L, Vu AT. Zoomed resolution in simultaneous multi-slice EPI for fMRI. In: Proceedings of the 21st Annual Meeting of ISMRM. Salt Lake City, UT. 2013:3316.
25. Setsompop K, Feinberg DA, Polimeni JR. Rapid brain MRI acquisition techniques at ultra-high fields. *NMR Biomed*. 2016;29:1198-1221.
26. Butts K, Riederer SJ, Ehman RL, Thompson RM, Jack CR. Interleaved echo planar imaging on a standard MRI system. *Magn Reson Med*. 1994;31:67-72.
27. Menon RS, Goodyear BG. Submillimeter functional localization in human striate cortex using BOLD contrast at 4 Tesla: Implications for the vascular point-spread function. *Magn Reson Med*. 1999;41:230-235.
28. Cheng K, Waggoner RA, Tanaka K. Human ocular dominance columns as revealed by high-field functional magnetic resonance imaging. *Neuron*. 2001;32:359-374.
29. Yacoub E, Shmuel A, Pfeuffer J, et al. Imaging brain function in humans at 7 Tesla. *Magn Reson Med*. 2001;45:588-594.
30. Goodyear BG, Menon RS. Brief visual stimulation allows mapping of ocular dominance in visual cortex using fMRI. *Hum Brain Mapp*. 2001;14:210-217.
31. Harel N, Lin J, Moeller S, Ugurbil K, Yacoub E. Combined imaging-histological study of cortical laminar specificity of fMRI signals. *NeuroImage*. 2006;29:879-887.
32. Goense J, Merkle H, Logothetis NK. High-resolution fMRI reveals laminar differences in neurovascular coupling between positive and negative BOLD responses. *Neuron*. 2012;76:629-639.
33. Menon RS, Thomas CG, Gati JS. Investigation of BOLD contrast in fMRI using multi-shot EPI. *NMR Biomed*. 1997;10:179-182.
34. Reeder SB, Atalar E, Bolster BD Jr, McVeigh ER. Quantification and reduction of ghosting artifacts in interleaved echo-planar imaging. *Magn Reson Med*. 1997;38:429-439.

35. Chapman B, Turner R, Ordidge RJ, et al. Real-time movie imaging from a single cardiac cycle by NMR. *Magn Reson Med*. 1987;5:246-254.
36. Polimeni JR, Bhat H, Witzel T, et al. Reducing sensitivity losses due to respiration and motion in accelerated echo planar imaging by reordering the autocalibration data acquisition. *Magn Reson Med*. 2016;75:665-679.
37. Mansfield P. Spatial mapping of the chemical shift in NMR. *Magn Reson Med*. 1984;1:370-386.
38. Kerr AB, Pauly JM, Nishimura DG. Slice profile stabilization for segmented k-space imaging. In: Proceedings of the 3rd Annual Meeting of SMRM. New York, NY. 1993. p. 1189.
39. Kerr AB, Pauly JM, inventors; Board of Trustees of the Leland Stanford Junior University, assignee. Slice profile stabilization for segmented k-space magnetic resonance imaging. US Patent 5,499,629. March 19, 1996.
40. Kim SG, Hu X, Adriany G, Ugurbil K. Fast interleaved echo-planar imaging with navigator: High resolution anatomic and functional images at 4 Tesla. *Magn Reson Med*. 1996;35:895-902.
41. Kang DH, Oh SH, Chung JY, Kim DE, Ogawa S, Cho ZH. A correction of amplitude variation using navigators in an interleave-type multi-shot EPI at 7T. In: Proceedings of the 19th Annual Meeting of ISMRM. Montreal, Canada; 2011. p. 4574.
42. Kang D-H, Chung J-Y, Kim D-E, Kim Y-B, Cho Z-H. A modified variable fip angle using a predefined slice profile in a consecutive interleaved EPI. In: Proceedings of the 20th Annual Meeting of ISMRM. Melbourne, Australia; 2012. p. 2453.
43. Deppe MH, Teh K, Parra-Robles J, Lee KJ, Wild JM. Slice profile effects in 2D slice-selective MRI of hyperpolarized nuclei. *J Magn Reson*. 2010;202:180-189.
44. Pauly J, Leroux P, Nishimura D, Macovski A. Parameter relations for the Shinnar-Leroux selective excitation pulse design algorithm. *IEEE Trans Med Imaging*. 1991;10:53-65.
45. Berman AJL, Witzel T, Grissom WAG, Park D, Setsompop K, Polimeni JR. High-resolution segmented-accelerated EPI using variable flip angle FLEET with tailored slice profiles. In: Proceedings of the 27th Annual Meeting of ISMRM. Montreal, Canada; 2019. p. 1169.
46. Feinberg DA, Oshio K. Phase errors in multi-shot echo planar imaging. *Magn Reson Med*. 1994;32:535-539.
47. Yarnykh VL. Actual flip-angle imaging in the pulsed steady state: A method for rapid three-dimensional mapping of the transmitted radiofrequency field. *Magn Reson Med*. 2007;57:192-200.
48. Feiweier T, inventor. Magnetic resonance method and apparatus to determine phase correction parameters. US Patent 20110234221. September 29, 2011.
49. Cox RW. AFNI: What a long strange trip it's been. *NeuroImage*. 2012;62:743-747.
50. Jenkinson M, Beckmann CF, Behrens TE, Woolrich MW, Smith SM. Fsl. *Neuroimage*. 2012;62:782-790.
51. Rooney WD, Johnson G, Li X, et al. Magnetic field and tissue dependencies of human brain longitudinal 1H2O relaxation in vivo. *Magn Reson Med*. 2007;57:308-318.
52. Polders DL, Leemans A, Luijten PR, Hoogduin H. Uncertainty estimations for quantitative in vivo MRI T1 mapping. *J Magn Reson*. 2012;224:53-60.
53. Ashburner J. SPM: A history. *NeuroImage*. 2012;62:791-800.
54. Smith SM. Fast robust automated brain extraction. *Hum Brain Mapp*. 2002;17:143-155.
55. Woolrich MW, Ripley BD, Brady M, Smith SM. Temporal autocorrelation in univariate linear modeling of FMRI data. *NeuroImage*. 2001;14:1370-1386.
56. Reuter M, Rosas HD, Fischl B. Highly accurate inverse consistent registration: A robust approach. *NeuroImage*. 2010;53:1181-1196.
57. Setsompop K, Gagoski BA, Polimeni JR, Witzel T, Wedeen VJ, Wald LL. Blipped-controlled aliasing in parallel imaging for simultaneous multislice echo planar imaging with reduced g-factor penalty. *Magn Reson Med*. 2012;67:1210-1224.
58. Polimeni JR, Setsompop K, Gagoski BA, McNab JA, Triantafyllou C, Wald LL. Rapid multi-shot segmented EPI using the simultaneous multi-slice acquisition method. In: Proceedings of the 20th Annual Meeting of ISMRM. Melbourne, Australia; 2012. p. 2222.
59. Wong EC. Optimized phase schedules for minimizing peak RF power in simultaneous multi-slice RF excitation pulses. In: Proceedings of the 20th Annual Meeting of ISMRM. Melbourne, Australia; 2012. p. 2209.
60. Cauley SF, Polimeni JR, Bhat H, Wald LL, Setsompop K. Interslice leakage artifact reduction technique for simultaneous multislice acquisitions. *Magn Reson Med*. 2014;72:93-102.
61. Constantinides CD, Atalar E, McVeigh ER. Signal-to-noise measurements in magnitude images from NMR phased arrays. *Magn Reson Med*. 1997;38:852-857.
62. Hoge WS, Polimeni JR. Dual-polarity GRAPPA for simultaneous reconstruction and ghost correction of echo planar imaging data. *Magn Reson Med*. 2016;76:32-44.
63. McKinnon GC. Ultrafast interleaved gradient-echo-planar imaging on a standard scanner. *Magn Reson Med*. 1993;30:609-616.
64. Kang DH, Chung JY, Kim DE, Kim YB, Cho ZH. Combination of consecutive interleaved EPI schemes and parallel imaging technique. In: Proceedings of the 20th Annual Meeting of ISMRM. Melbourne, Australia; 2012. p. 4175.
65. Hetzer S, Mildner T, Moller HE. A modified EPI sequence for high-resolution imaging at ultra-short echo time. *Magn Reson Med*. 2011;65:165-175.
66. Fracasso A, Luijten PR, Dumoulin SO, Petridou N. Laminar imaging of positive and negative BOLD in human visual cortex at 7 T. *NeuroImage*. 2018;164:100-111.
67. Boxerman JL, Hamberg LM, Rosen BR, Weisskoff RM. MR contrast due to intravascular magnetic-susceptibility perturbations. *Magn Reson Med*. 1995;34:555-566.
68. Polimeni JR, Renvall V, Zaretskaya N, Fischl B. Analysis strategies for high-resolution UHF-fMRI data. *NeuroImage*. 2018;168:296-320.
69. Blazejewska AI, Fischl B, Wald LL, Polimeni JR. Intracortical smoothing of small-voxel fMRI data can provide increased detection power without spatial resolution losses compared to conventional large-voxel fMRI data. *NeuroImage*. 2019;189:601-614.
70. Grissom WA, Sacolick L, Vogel MW. Improving high-field MRI using parallel excitation. *Imaging Med*. 2010;2:675-693.
71. Gras V, Boland M, Vignaud A, et al. Homogeneous non-selective and slice-selective parallel-transmit excitations at 7 Tesla with universal pulses: A validation study on two commercial RF coils. *PLoS ONE*. 2017;12:1-16.
72. Chen NK, Guidon A, Chang HC, Song AW. A robust multi-shot scan strategy for high-resolution diffusion weighted MRI enabled by multiplexed sensitivity-encoding (MUSE). *NeuroImage*. 2013;72:41-47.

73. Mani M, Jacob M, Kelley D, Magnotta V. Multi-shot sensitivity-encoded diffusion data recovery using structured low-rank matrix completion (MUSSELS). *Magn Reson Med*. 2017;78:494-507.
74. Huber L, Handwerker DA, Jangraw DC, et al. High-resolution CBV-fMRI allows mapping of laminar activity and connectivity of cortical input and output in human M1. *Neuron*. 2017;96:1253-1263.e7.
75. Kashyap S, Ivanov D, Havlicek M, Sengupta S, Poser BA, Uludag K. Resolving laminar activation in human V1 using ultra-high spatial resolution fMRI at 7T. *Sci Rep*. 2018;8:17063.
76. Feinberg DA, Moeller S, Smith SM, et al. Multiplexed echo planar imaging for sub-second whole brain FMRI and fast diffusion imaging. *PLoS ONE*. 2010;5:1-11.
77. Chen JE, Polimeni JR, Bollmann S, Glover GH. On the analysis of rapidly sampled fMRI data. *NeuroImage*. 2019;188:807-820.
78. Lewis LD, Setsompop K, Rosen BR, Polimeni JR. Stimulus-dependent hemodynamic response timing across the human subcortical-cortical visual pathway identified through high spatiotemporal resolution 7T fMRI. *NeuroImage*. 2018;181:279-291.
79. Breuer FA, Blaimer M, Heidemann RM, Mueller MF, Griswold MA, Jakob PM. Controlled aliasing in parallel imaging results in higher acceleration (CAIPIRINHA) for multi-slice imaging. *Magn Reson Med*. 2005;53:684-691.
80. Keil B, Blau JN, Biber S, et al. A 64-channel 3T array coil for accelerated brain MRI. *Magn Reson Med*. 2013;70:248-258.
81. Uğurbil K, Auerbach E, Moeller S, et al. Brain imaging with improved acceleration and SNR at 7 Tesla obtained with 64-channel receive array. *Magn Reson Med*. 2019;82:495-509.
82. Dai E, Ma X, Zhang Z, Yuan C, Guo H. Simultaneous multislice accelerated interleaved EPI DWI using generalized blipped-CAIPI acquisition and 3D K-space reconstruction. *Magn Reson Med*. 2017;77:1593-1605.
83. Setsompop K, Cohen-Adad J, Gagoski BA, et al. Improving diffusion MRI using simultaneous multi-slice echo planar imaging. *NeuroImage*. 2012;63:569-580.
84. Berman AJL, Grissom WA, Witzel T, et al. Segmented spin-echo BOLD fMRI using a variable flip angle FLEET acquisition with recursive RF pulse design for high spatial resolution fMRI. In: Proceedings of 28th Annual Meeting of ISMRM. Paris, France; 2020. p. 5236.
85. Poser BA, Koopmans PJ, Witzel T, Wald LL, Barth M. Three dimensional echo-planar imaging at 7 Tesla. *NeuroImage*. 2010;51:261-266.
86. Lutti A, Thomas DL, Hutton C, Weiskopf N. High-resolution functional MRI at 3 T: 3D/2D echo-planar imaging with optimized physiological noise correction. *Magn Reson Med*. 2013;69:1657-1664.
87. Jorge J, Figueiredo P, van der Zwaag W, Marques JP. Signal fluctuations in fMRI data acquired with 2D-EPI and 3D-EPI at 7 Tesla. *Magn Reson Imaging*. 2013;31:212-220.
88. Huber L, Ivanov D, Handwerker DA, et al. Techniques for blood volume fMRI with VASO: From low-resolution mapping towards sub-millimeter layer-dependent applications. *NeuroImage*. 2018;164:131-143.
89. Le Ster C, Moreno A, Mauconduit F, et al. Comparison of SMS-EPI and 3D-EPI at 7T in an fMRI localizer study with matched spatiotemporal resolution and homogenized excitation profiles. *PLoS ONE*. 2019;14:1-17.
90. Gai ND, Talagala SL, Butman JA. Whole-brain cerebral blood flow mapping using 3D echo planar imaging and pulsed arterial tagging. *J Magn Reson Imaging*. 2011;33:287-295.
91. Van Der Zwaag W, Marques JP, Kober T, Glover G, Gruetter R, Krueger G. Temporal SNR characteristics in segmented 3D-EPI at 7T. *Magn Reson Med*. 2012;67:344-352.

SUPPORTING INFORMATION

Additional Supporting Information may be found online in the Supporting Information section.

FIGURE S1 Effect of the number of shots (S) vs. acceleration factor (R) on image quality and SNR at 0.8 mm isotropic at 7 T. From top to bottom, the shots increase from 1 to 3 while the acceleration decreases from 6 to 2 such that the undersampling per shot, $U_{SR} = S \times R$, equals 6 in all cases. (A)-(C) show a single repetition's axial slice and corresponding sagittal reformat; (D)-(F) show maps of tSNR; (G)-(I) show maps of the calculated well-conditioned SNR ($\text{SNR}_{\text{g-free}} = \text{SNR} \times g$); and (J)-(L) show the calculated inverse g-factor maps. For all three acquisitions, the volume TR was matched by adjusting the slice coverage. The values in angle brackets in the top-right of each map provide the average value across a whole-brain mask that is common to all three acquisitions. The tSNR and $\text{SNR}_{\text{g-free}}$ maps share the colour bar centered beneath them and the $1/g$ maps use the colour bar beneath them

FIGURE S2 Simulated steady-state VFA-FLEET-SLR slice profiles across shots accounting for T_1 relaxation between segments and between repetitions. The slice profile magnitudes for two- and three-shot sequences are shown for $T_1 = 600$ ms (A,E), 1500 ms (B,F), and 3000 ms (C,G), and the integrated slice profile magnitudes are compared (D,H). The simulations assumed segment TR = 60 ms and volume TR = $S \times 2000$ ms (ie, 4000 ms and 6000 ms). The curves in (D) and (H) are labeled with the corresponding T_1 values

FIGURE S3 The impact of B_1^+ variation on the simulated VFA-FLEET-SLR slice profiles. Magnitude and phase slice profiles are shown for $B_1/B_{1,\text{nom}} = 0.7$, 1.0, and 1.3 (A–F,I–N), with the two-shot sequence on top and the three-shot sequence on the bottom. The integrated slice profile magnitudes across shots are plotted as a function of the B_1^+ ratio (G,O) along with the norm of the difference between slice profiles relative to the first shot (H,P). Rather than label the shots by flip angle, they have been labeled S1 for shot 1, S2 for shot 2, and so on. For display purposes, the plotted phase is set to zero wherever $|M_{xy}| < 0.02$

FIGURE S4 Simulated image reconstruction demonstrating the impact of B_1^+ non-uniformity on ghosting in two-shot VFA-FLEET-SLR. (A) Relative B_1^+ map where the nominal flip angle is achieved in the periphery of the brain. (B) Histogram of B_1^+ values throughout the brain. Reconstructed image (C) without and (D) with inter-segment magnitude normalization. The right halves of (C) and (D) have been scaled by a factor of five to emphasize the ghosting. (E) and (F) show the differences of the reconstructed images in (C) and (D), respectively, with the non-ghosted reference image. (C)-(F) have been normalized by the mean whole-brain intensity in the reference image

FIGURE S5 Simulated image reconstruction demonstrating the impact of B_1^+ non-uniformity on ghosting in two-shot VFA-FLEET-SLR. (A) Relative B_1^+ map where the nominal flip angle is achieved in the centre of the brain. (B) Histogram of B_1^+ values throughout the brain. Reconstructed image (C) without and (D) with inter-segment magnitude normalization. The right halves of (C) and (D) have been scaled by a factor of five to emphasize the ghosting. (E) and (F) show the differences of the reconstructed images in (C) and (D), respectively, with the non-ghosted reference image. (C)-(F) have been normalized by the mean whole-brain intensity in the reference image

FIGURE S6 Simulated impact of RF pulse type on image reconstruction and tSNR in a uniform digital phantom. The simulated image formation and reconstruction process was performed for VFA-FLEET using scaled sinc pulses (A and C) and the proposed recursive SLR pulses (B and D) for two shots (top row) and three shots (bottom row). The mean reconstructed images are shown on the left of each panel and the tSNR maps are shown on the right, all with matching colour scales. Aliasing artifacts are apparent in the reconstructions and tSNR maps using the scaled sinc pulses but are not present when using the recursive SLR pulses. Due to the broadening of the VFA-FLEET-Sinc slice profile, its tSNR is 7% greater for two shots and 13% greater for three shots as compared to VFA-FLEET-SLR

FIGURE S7 Flowchart of the simultaneous multi-slice image reconstruction for VFA-FLEET. Prior to training (application) of the slice-GRAPPA kernels, intra-segment Nyquist ghost correction was applied to the calibration (imaging) data using the slice-group average collapsed calibration (imaging) navigators. After unaliasing of the collapsed slices, the slice-group average ghost correction was subtracted and replaced by the slice-specific intra- and inter-segment ghost corrections (phase and magnitude). These slice-specific corrections were derived from the navigators of the calibration data

TABLE S1 VFA-FLEET-SLR acquisition parameters chosen for experiments comparing the trade-off between segmentation and acceleration

VIDEO S1 Demonstration of two-shot, unaccelerated, conventional-segmented EPI, VFA-FLEET-Sinc, and VFA-FLEET-SLR in a single subject (subject 1) at 3 T. Every other repetition out of 60 is displayed without inter-segment normalization. This subject exhibited motion that resulted in severe intermittent ghosting artifacts in the conventional-segmented acquisition, whereas the VFA-FLEET acquisitions were relatively stable. Stable ghosting in VFA-FLEET-Sinc is present in all repetitions. Note that, due to the motion levels, all scans from this subject were excluded from further analyses

VIDEO S2 Demonstration of two-shot, unaccelerated, conventional-segmented EPI, VFA-FLEET-Sinc, and VFA-FLEET-SLR in a single subject (subject 3, same subject as shown in Figure 3) at 3 T. Every other repetition out of 60 is displayed without inter-segment normalization. This subject exhibited little motion, resulting in stable imaging in all acquisitions. Stable ghosting in VFA-FLEET-Sinc is present in all repetitions

VIDEO S3 Demonstration of three-shot, unaccelerated, conventional-segmented EPI, VFA-FLEET-Sinc, and VFA-FLEET-SLR in a single subject (subject 1) at 3 T. Every other repetition out of 60 is displayed without inter-segment normalization. This subject exhibited motion that resulted in severe intermittent ghosting artifacts in the conventional-segmented acquisition, whereas the VFA-FLEET acquisitions were relatively stable. Stable ghosting in VFA-FLEET-Sinc is present in all repetitions. Note that due to the motion levels, all scans from this subject were excluded from further analyses

VIDEO S4 Demonstration of three-shot, unaccelerated, conventional-segmented EPI, VFA-FLEET-Sinc, and VFA-FLEET-SLR in a single subject (subject 3, same subject as shown in Figure 3) at 3 T. Every other repetition out of 60 is displayed without inter-segment normalization. This subject exhibited little motion, resulting in stable imaging in all acquisitions. Stable ghosting in VFA-FLEET-Sinc is present in all repetitions

VIDEO S5 Demonstration of two-shot, $R = 4$, 1-mm isotropic conventional-segmented EPI, VFA-FLEET-Sinc, and VFA-FLEET-SLR in a single subject (subject 6) at 7 T. Every other repetition out of 60 is displayed without inter-segment normalization. This subject had negligible motion, however, the conventional-segmented acquisition still exhibited intermittent ghosting, presumably due to B_0-induced fluctuations from respiration, whereas the VFA-FLEET acquisitions were relatively stable. Stable ghosting, manifesting as unresolved aliasing and bands or broad regions of signal dropout, is present to a greater extent in VFA-FLEET-Sinc than in VFA-FLEET-SLR

VIDEO S6 Demonstration of two-shot, $R = 4$, 1-mm isotropic conventional-segmented EPI, VFA-FLEET-Sinc, and VFA-FLEET-SLR in a single subject (subject 9, same subject as shown in Figure 4) at 7 T. Every other repetition out of 60 is displayed without inter-segment normalization. The conventional-segmented acquisition exhibited intermittent ghosting during periods of negligible motion, presumably due to B_0-induced fluctuations from respiration, and increased ghosting during head motion. The VFA-FLEET acquisitions were relatively stable. Stable ghosting, manifesting as unresolved aliasing and bands or broad regions of signal dropout, is present to a greater extent in VFA-FLEET-Sinc than in VFA-FLEET-SLR

VIDEO S7 Demonstration of three-shot, $R = 4$, 1-mm isotropic conventional-segmented EPI, VFA-FLEET-Sinc, and VFA-FLEET-SLR in a single subject (subject 6) at 7 T. Every other repetition out of 60 is displayed without inter-segment normalization. This subject had negligible motion, however, the conventional-segmented acquisition still exhibited intermittent ghosting, presumably due to B_0-induced fluctuations from respiration, whereas the VFA-FLEET acquisitions were relatively stable. Stable ghosting, manifesting as unresolved aliasing and bands or broad regions of signal dropout, is present to a greater extent in VFA-FLEET-Sinc than in VFA-FLEET-SLR

VIDEO S8 Demonstration of three-shot, $R = 4$, 1-mm isotropic conventional-segmented EPI, VFA-FLEET-Sinc, and VFA-FLEET-SLR in a single subject (subject 9, same subject as shown in Figure 4) at 7 T. Every other repetition out of 60 is displayed without inter-segment normalization. The conventional-segmented acquisition exhibited intermittent ghosting during periods of negligible motion, presumably due to B_0-induced fluctuations from respiration, and intensified ghosting during head motion. The VFA-FLEET acquisitions were relatively stable. Stable ghosting, manifesting as unresolved aliasing and bands or broad regions of signal dropout, is present to a greater extent in VFA-FLEET-Sinc than in VFA-FLEET-SLR

How to cite this article: Berman AJL, Grissom WA, Witzel T, et al. Ultra-high spatial resolution BOLD fMRI in humans using combined segmented-accelerated VFA-FLEET with a recursive RF pulse design. *Magn Reson Med*. 2020;00:1–20. https://doi.org/10.1002/mrm.28415